Acta Cryst. (1982). A**38**, 55–61

Three-Dimensional Strain-Field Information in Convergent-Beam Electron Diffraction Patterns

BY R. W. CARPENTER*

Metals and Ceramics Division, Oak Ridge National Laboratory, Oak Ridge, Tennessee 37830, *USA*

AND J. C. H. SPENCE

Department of Physics, Arizona State University, Tempe, Arizona 85281, *USA*

(*Received* 20 *November* 1979; *accepted* 20 *June* 1980)

Abstract

Convergent-beam electron diffraction (CBED) patterns contain diffracted beams from higher-order Laue zones (HOLZ), in addition to the more often observed diffracted beams from the zeroth-order reciprocal-lattice zone (ZOLZ) that contains the origin of the reciprocal lattice. Since HOLZ diffraction vectors have non-zero components along the incident electron beam direction, they can detect components of static real-lattice displacement fields that lie along the incident electron beam direction, an event not possible for diffracted beams normal to the incident electron beam direction (*i.e.* ZOLZ diffracted beams). This effect is used in the present work to determine Burgers vectors of straight dislocations and loops in silicon from observations of splitting of HOLZ lines within the forward scattered beam Bragg disk, and from splitting of Kikuchi lines associated with HOLZ Bragg reflections. The method was also applied with limited success to dislocations in aluminum; here splitting was more difficult to observe because of the rather strong diffuse background in the CBED patterns. Calculations of HOLZ line splitting due to the presence of a dislocation in the irradiated crystal volume were in good qualitative agreement with the experimental observations. Effects on CBED patterns to be expected from some partial dislocations are discussed. This CBED method can be very useful for the determination of non-ZOLZ fault vector components in an atomic-resolution structure-imaging microscope. These instruments usually have specimen tilt ranges limited to about 10°; thus conventional Burgers-vector analysis is not generally possible. Finally, the present CBED results show clearly that the projection approximation generally used to interpret structure fringe images is not strictly valid. The changes in fringe images or weak-beam images from HOLZ excitations remain to be evaluated.

*Present address: ASU Facility for High Resolution Electron Microscopy, Center for Solid State Science, Arizona State University, Tempe, Arizona 85281, USA.

0567-7394/82/010055-07$01.00

© 1982 International Union of Crystallography

1. Introduction

The two-dimensional nature of electron diffraction at high energies has generally been regarded as a major limitation of the technique. Thus, in any analysis based on the projection or zero-order Laue zone (ZOLZ) approximation, diffraction patterns, diffraction contrast images and high-resolution lattice images are all insensitive to the movement of atoms (or strain-field components) in the direction of the electron beam. Much recent work has been devoted to the development of techniques which allow three-dimensional information (such as crystal symmetry or surface imperfections) to be extracted from a single transmission electron micrograph rather than from stereo pairs (Cherns, 1974; Goodman, 1975; Jones, Rackham & Steeds, 1977; Rackham & Steeds, 1976). Most of this work has been devoted to perfect crystals. In this paper we discuss an investigation into the usefulness of convergent-beam electron diffraction patterns (CBED) for the determination of dislocation Burgers vectors. Our aim has been to develop a method whereby, through the use of higher-order Laue-zone (HOLZ) interactions, a single zone-axis convergent-beam pattern can be used to find any arbitrary Burgers vector, without restriction to the plane normal to the electron beam. Experimental results are given, and it is shown that this is possible for a limited number of cases. In addition, a method is described which allows the form of HOLZ lines to be computed from imperfect crystals, using the column approximation.

2. Experimental details

2.1. *Specimen materials*

Dislocations in two materials, single-crystal silicon and polycrystalline aluminum, were examined. The silicon was semiconductor grade (from Motorola, Inc., Phoenix, Arizona), sliced into disks with [111] cylinder axis. After slicing, the disks were heated in an argon

atmosphere to 1273 K and a point load sufficient to cause plastic deformation was applied along [111]. The load was then removed and the disk cooled to room temperature, after which it was chemically thinned to electron transparency.

Aluminum specimens were prepared by punching 3 mm diameter disks from 1100 grade (commercial purity) sheet stock. The disks were recrystallized (1 h at 673 K) after punching and then compressed ~3% at room temperature. After compression the disks were electrochemically thinned to transparency at room temperature.

2.2. *Electron microscopy*

All microscopy examinations were conducted in a Philips EM 400 TEM/STEM fitted with a field emission electron gun described elsewhere (Carpenter & Bentley, 1979). Convergent-beam diffraction patterns (CBED) were recorded on film in the TEM mode with the probe focused on the electron entrance surface of the specimen. Probe focus was controlled with the second condenser lens. The probe can be focused on the specimen by switching the microscope to diffraction mode and observing the detailed intensity distribution within the central Bragg disk. When the probe is not focused on the specimen a real space shadow image of the irradiated specimen area will be visible. As the second condenser lens current is changed to bring the probe to focus on the specimen, the magnification of the shadow image will increase. At probe focus the magnification becomes infinite and all real space detail in the shadow image is lost. To focus the probe on a lattice defect, such as a dislocation, the defect is observed in the shadow image during focusing with the second condenser and the position of the probe on the defect is maintained by adjustment of the beam deflection controls. A second condenser aperture of 150 μm diameter was used, which produced an illumination half-angle of 7 mrad at focus. The probe size at focus was estimated to be approximately 10 nm.

Dislocation Burgers vectors in silicon were determined by the usual image contrast method with ⟨111⟩, ⟨220⟩, and ⟨311⟩ diffraction vectors within 20° of the [111] foil normal. Larger tilts were necessary in polycrystalline aluminum, resulting in greater projected specimen thicknesses.

3. Experimental results

The effect of long-range strain on CBED patterns is to replace the fine Kikuchi and HOLZ lines (in the central disk) by sets of fine fringes parallel to the corresponding lines of the unstrained crystal. HOLZ lines within the central Bragg disk result from elastic scattering and Kikuchi lines outside the Bragg disks result from inelastic scattering. The geometry of the two patterns is very similar and the same geometric procedure is used for indexing both. The relationship between HOLZ and Kikuchi lines has been discussed qualitatively by Steeds (1979). If two unsplit Kikuchi or HOLZ lines (diffracted from non-parallel planes unaffected by the presence of the dislocation) can be found and indexed, the vector cross product of these indices is parallel to the dislocation Burgers vector. One of these lines may result from a HOLZ reflection.

The simplest splitting geometry observed in Kikuchi lines (and bands) and higher-order Laue-zone (HOLZ) lines resulted when the CBED probe was positioned approximately over an isolated straight dislocation. A typical example of Kikuchi band splitting for such a case is shown in Fig. 1, with a similar pattern from a perfect crystal region for comparison. Note the threefold symmetry of the perfect-crystal CBED pattern, which, through HOLZ interactions, expresses the threefold rotational symmetry of the [111] axis, rather than the sixfold ZOLZ symmetry. The dislocation in this case was a straight 60° dislocation in the plane of the foil with Burgers vector $\pm\frac{1}{2}[1\bar{1}0]$. Note that all Kikuchi lines – both those corresponding to in-zone and HOLZ Bragg reflections – except those parallel to the Burgers-vector direction (marked) are split. The Bragg reflections corresponding to unsplit Kikuchi lines satisfy the relation $\mathbf{g}.\mathbf{b} = 0$. Note that the weak $\mathbf{g}.\mathbf{b}$ (edge) term does not cause appreciable splitting of lines satisfying $\mathbf{g}.\mathbf{b} = 0$. HOLZ lines in the central disk were found to be split [Fig. 2(*a*)] by dislocations and unsplit from the perfect region of the crystal [Fig. 2(*b*)]. Note that the symmetry of the extinction contours in the central disk is also severely perturbed when the incident probe is positioned over a dislocation.

Experiments were also performed to determine the effect of the probe position relative to the dislocation image on the CBED patterns. The probe could be positioned relative to the dislocation in several ways: the beam could be focused on the dislocation image in the TEM mode and then the microscope switched to diffraction mode, or the probe could be approximately positioned on the dislocation image and then final positioning made by viewing the dislocation shadow image in the underfocused diffraction pattern as it is brought to focus. Near the diffraction pattern focus, extinction contours within the Bragg disks, HOLZ lines and Kikuchi bands were all seen to vary rapidly with focus when the probe was very close to a dislocation. The latter method was found most sensitive for positioning the probe close to a dislocation. The sharp splitting of HOLZ and Kikuchi lines [Fig. 1(*a*)] was only observable when the probe was very close to a dislocation. The coarser intensity asymmetry, most easily observable on low-index in-zone Kikuchi bands (*e.g.* ⟨220⟩), persisted for probe positions farther from the dislocation image (~100 nm) and was found to be

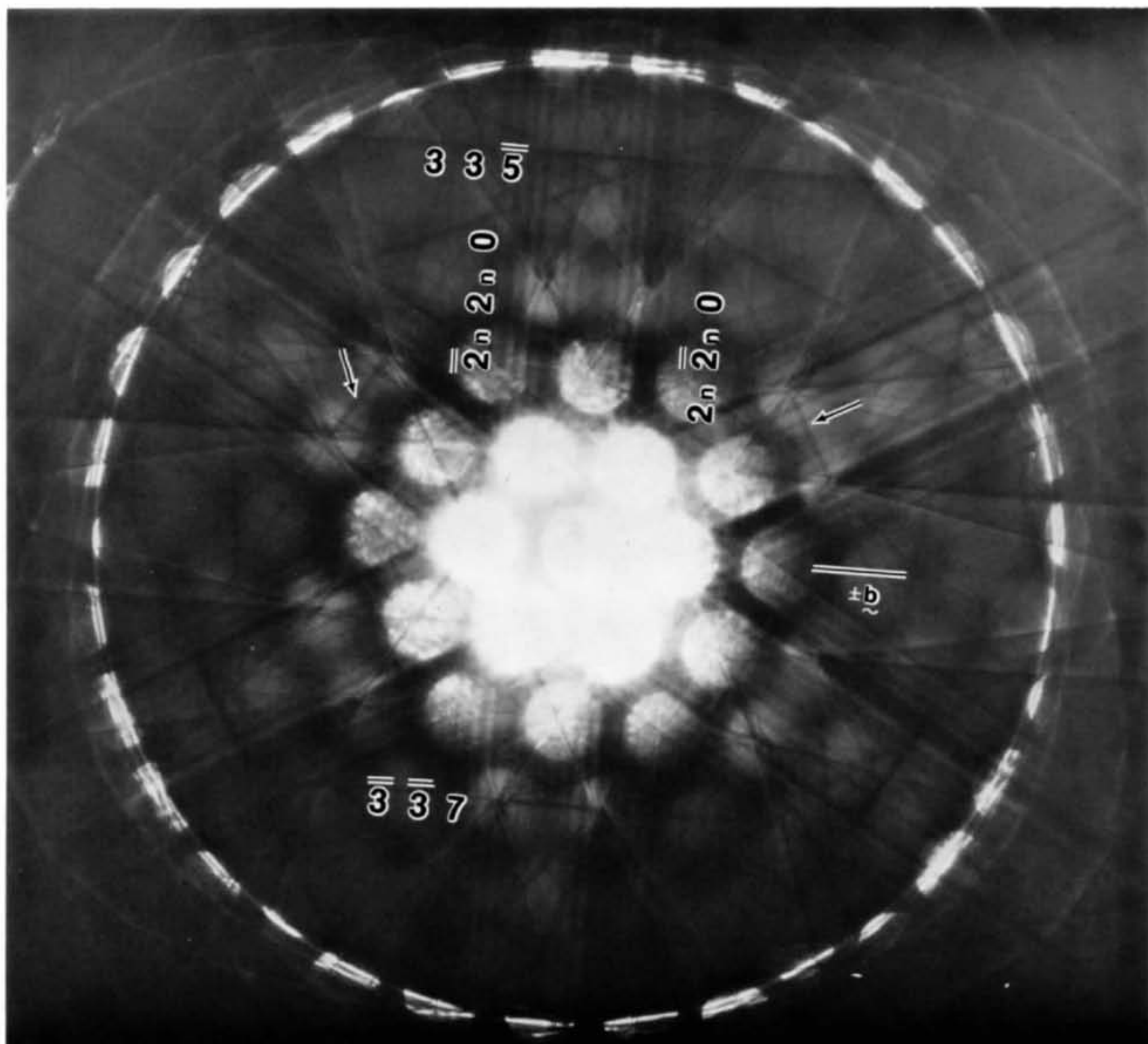

(*a*)

Fig. 1. (*a*) [111] zone-axis CBED pattern from a 60° dislocation in silicon. The dislocation Burgers vector lies in the [111] zone and is marked. Unsplit Kikuchi lines, both in the ZOLZ ± [22$\bar{4}$] and in the FOLZ [33$\bar{5}$] and [$\bar{3}\bar{3}$7] are indicated.

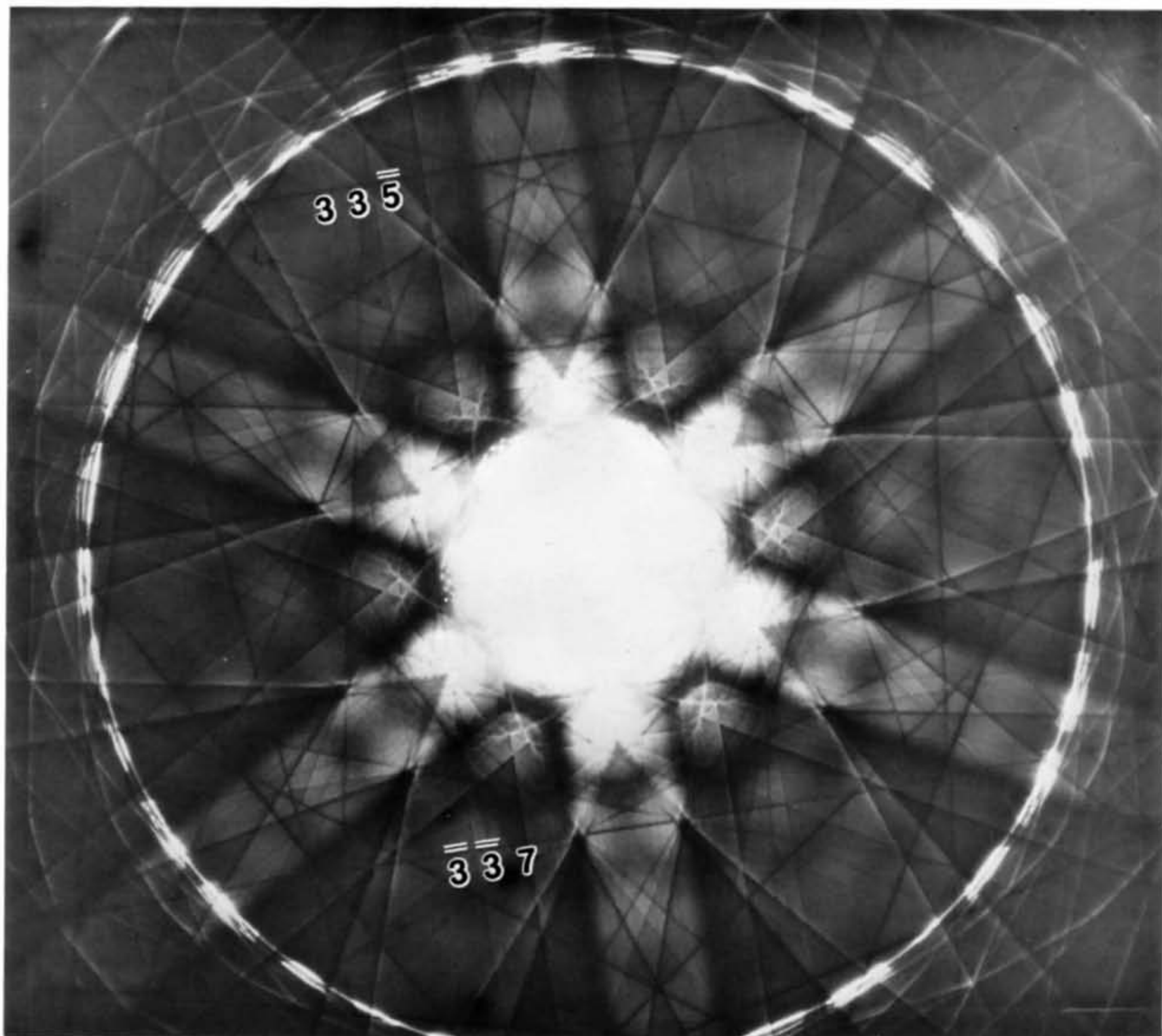

(*b*)

Fig. 1 (*cont.*). (*b*) Similar [111] zone-axis CBED pattern from perfectly crystalline silicon. All Kikuchi lines are sharp (unsplit). Note the reduction from sixfold to threefold symmetry due to HOLZ interactions. Both patterns taken at 120 kV.

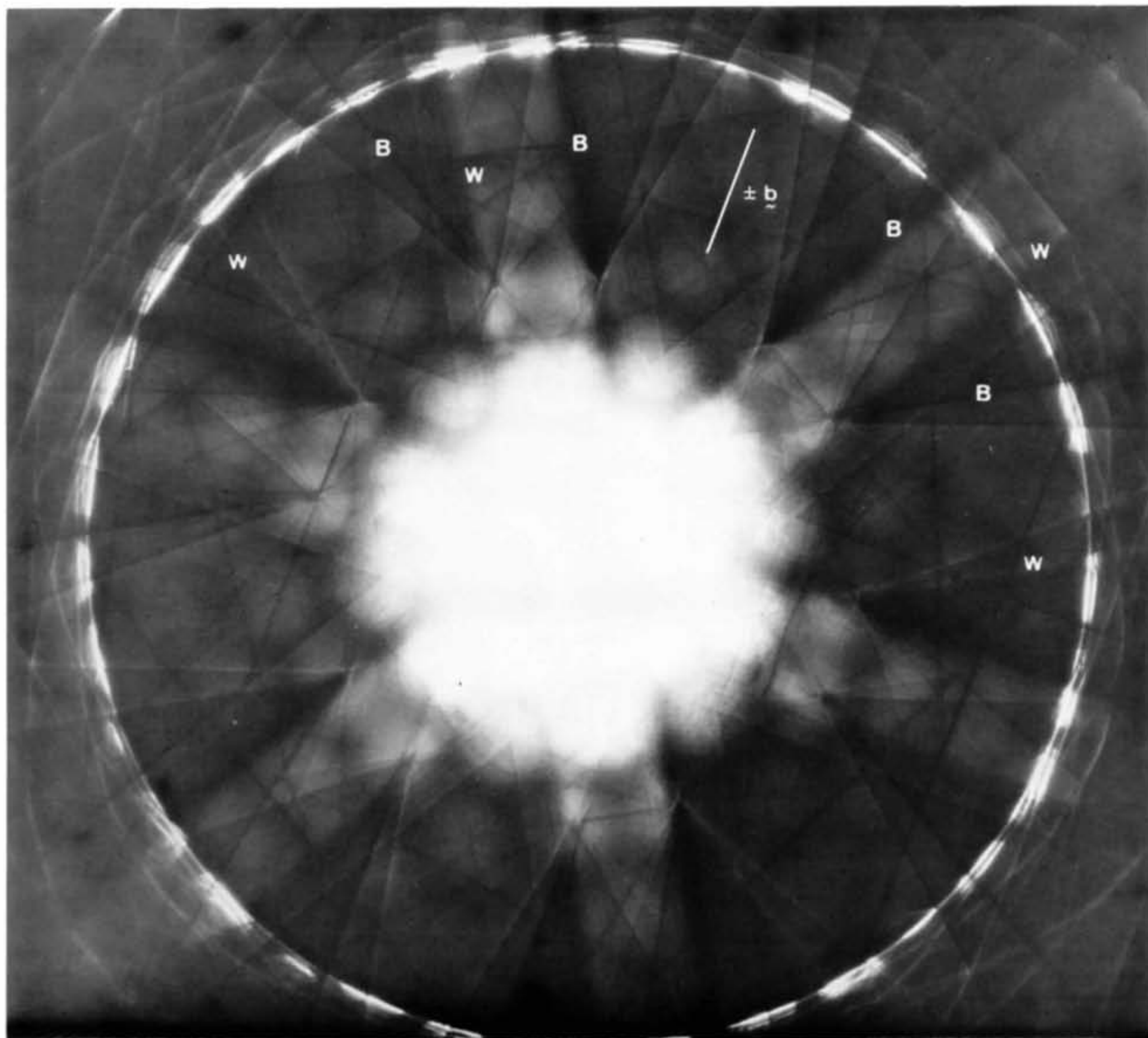

(a)

Fig. 3. The effect on low-index Kikuchi band intensity asymmetry when the probe is positioned to the right or left of a dislocation. The probe is to the left of the dislocation in (a) and to the right in (b). As the crystal planes tilt through the symmetric orientation, the 'excess' and 'defect' lines interchange [see Hirsch *et al.* (1965), p. 120]. The beam direction is **B** = [111], accelerating voltage 120 kV. The symbols indicate *W* (white) and *B* (black) lines.

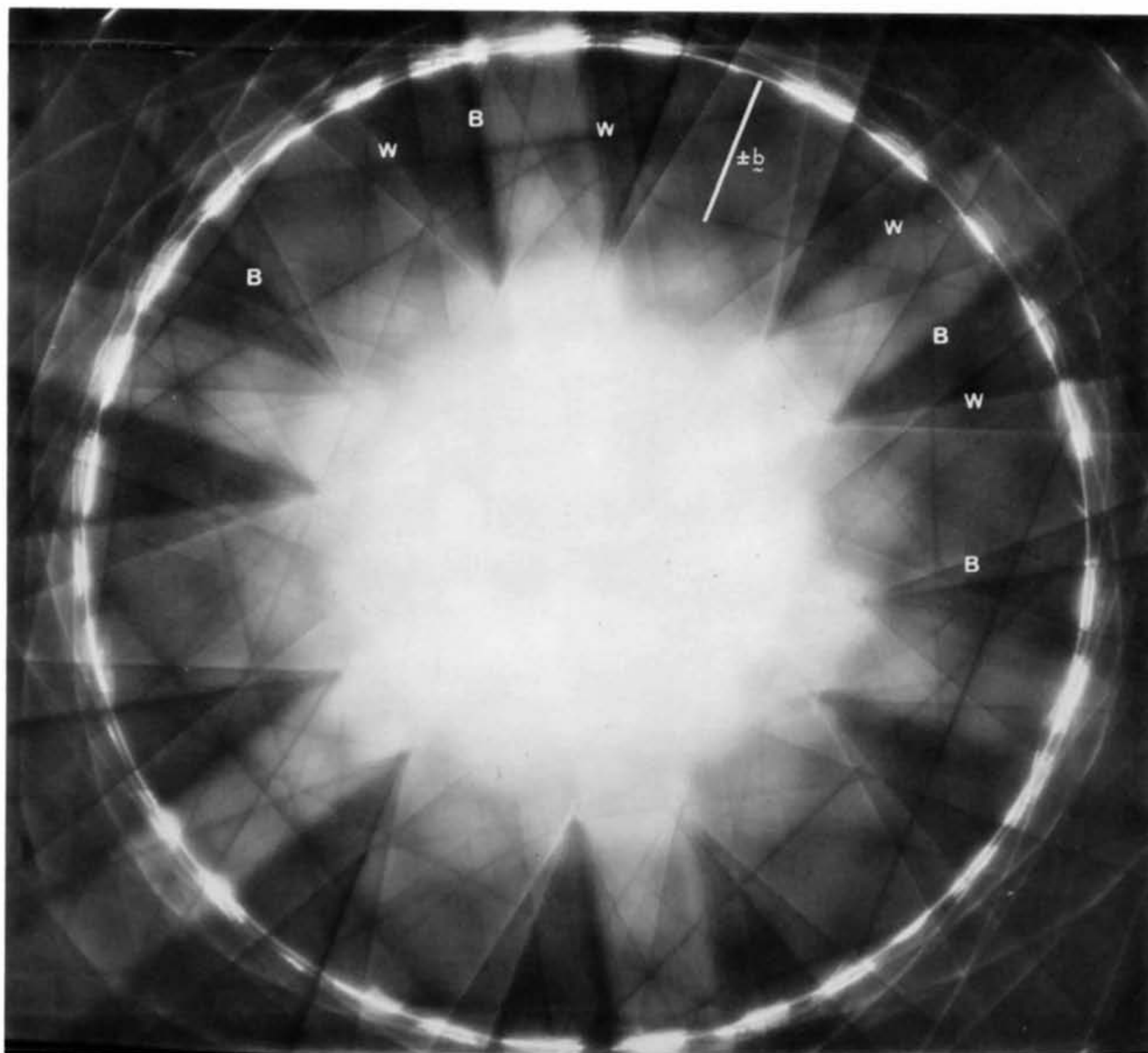

(b)

Fig. 3 (cont.)

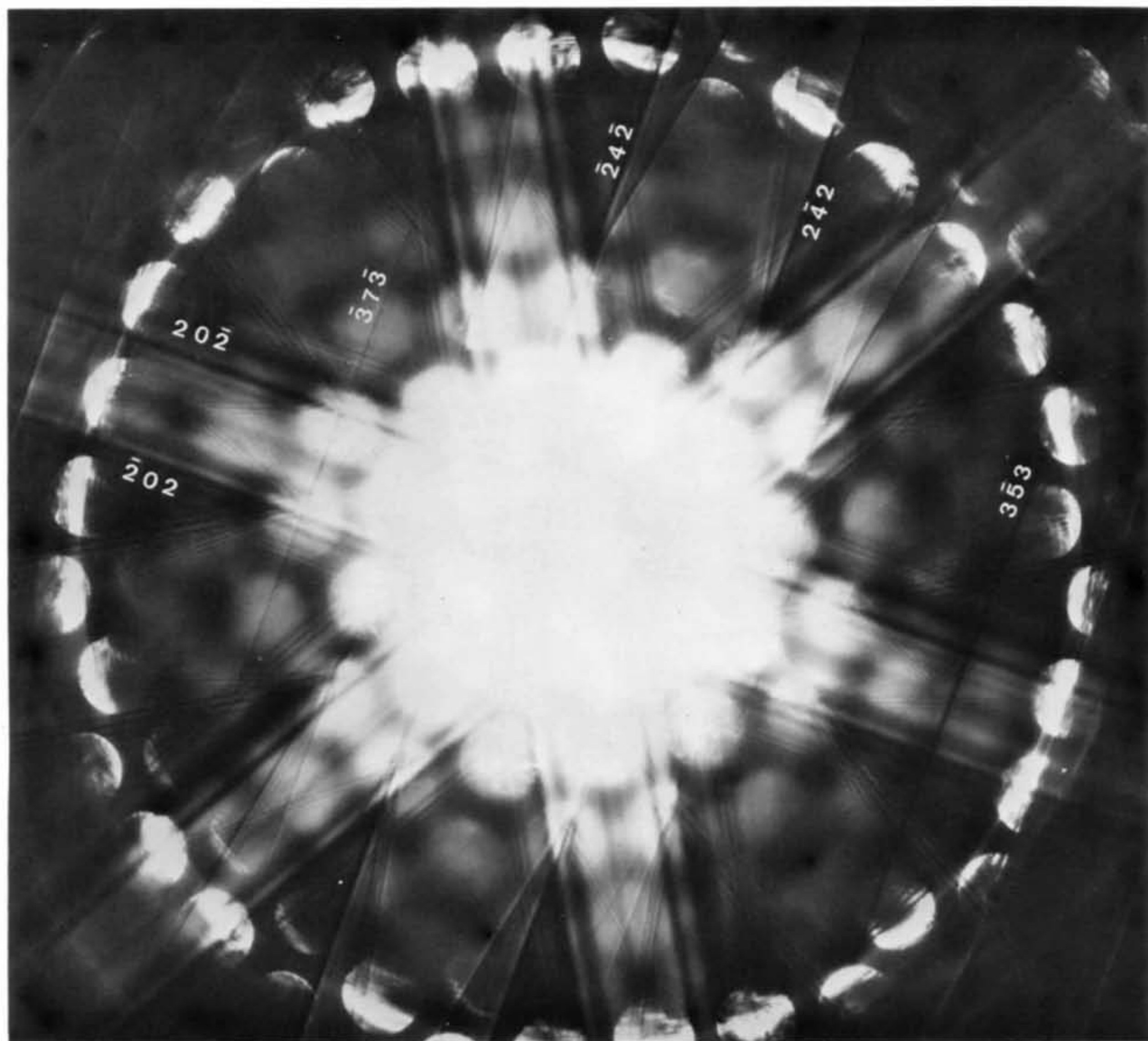

(*a*)

Fig. 5. CBED patterns from loop *A* of Fig. 4 for several incident beam directions. For loop *A*, $\mathbf{b} = \pm\frac{1}{2}[10\bar{1}]$. (*a*) $\mathbf{B} = [111]$, Kikuchi bands for $\pm[2\bar{4}2]$, $[3\bar{5}3]$ and $[\bar{3}7\bar{3}]$ are unsplit.

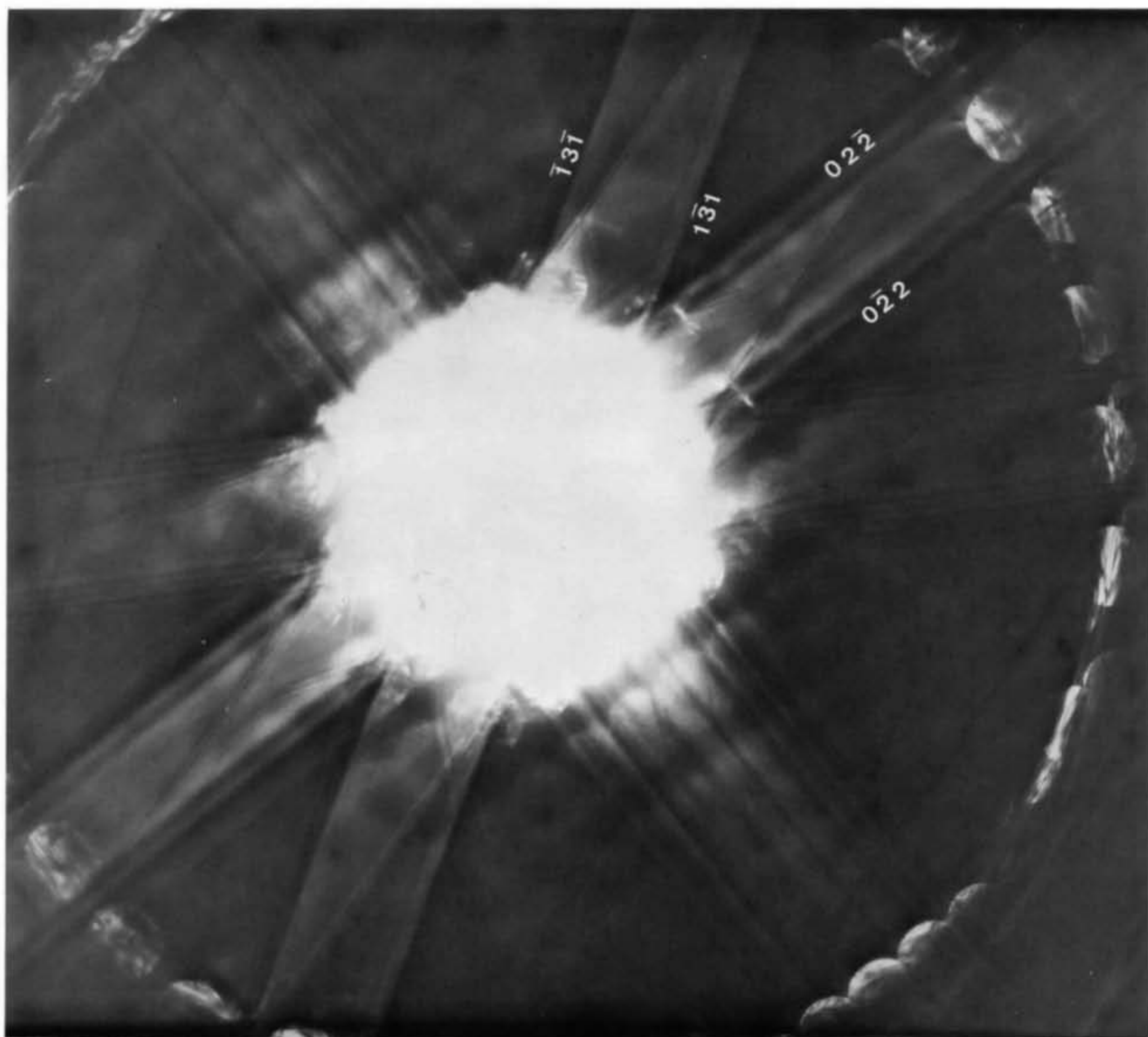

(*b*)

Fig. 5 (*cont.*). (*b*) $\mathbf{B} = [211]$, $\pm[1\bar{3}1]$ Kikuchi bands unsplit.

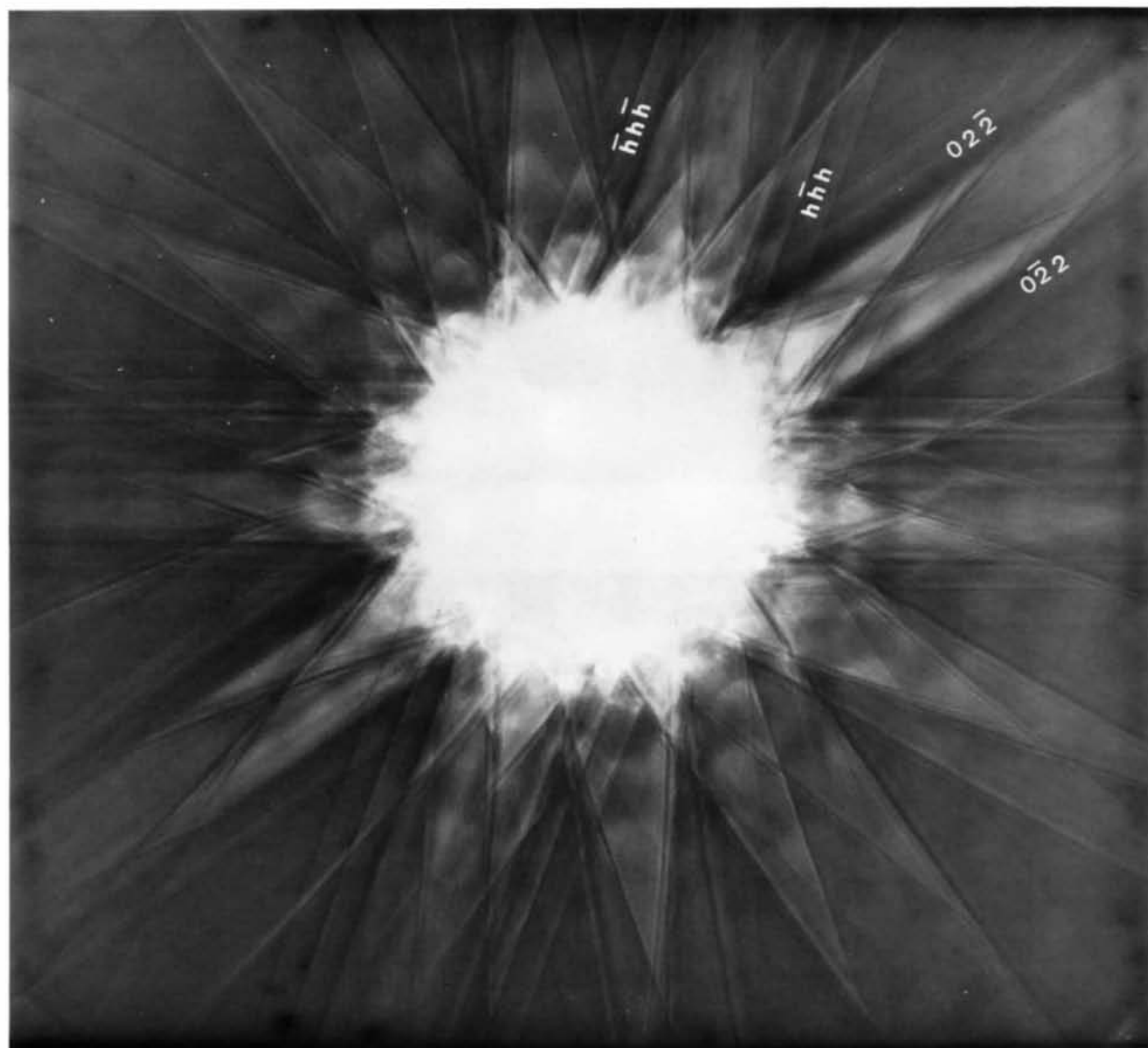

(*c*)

Fig. 5 (*cont.*). (*c*) $\mathbf{B} = [011]$, $\pm[h\bar{h}h]$ Kikuchi bands unsplit.

directly related to the position of the probe with respect to the dislocation. An example is shown in Fig. 3. Here CBED patterns were recorded with the probe positioned to the right and left of the dislocation. In both cases the probe is far enough away from the dislocation so that sharp splitting was difficult to observe; HOLZ and Kikuchi lines that would be sharply split if the probe were closer can be seen to be broadened in each case. But the intensity asymmetry, especially visible in $\langle 220 \rangle$ Kikuchi bands, is symmetric with respect to the Burgers-vector direction, which is marked on the figure. The **symmetry** reverses when the probe is moved from one side of the dislocation to the other. For example, with the probe on the left, the $[02\bar{2}]$ and $[2\bar{2}0]$ Kikuchi bands are weaker than the $[02\bar{2}]$ and $[\bar{2}20]$ bands. This symmetry is reversed if the probe is moved to the right of the dislocation. The effect is also present on higher-order Kikuchi bands such as $\langle 422 \rangle$, but is weaker and more difficult to observe. The effect results from the tilting of diffracting planes near the dislocation and can be used to identify the sense of **b**.

Several dislocation loops were also examined in silicon to determine whether splitting in CBED patterns corresponds with image invisibility experiments. Fig. 4

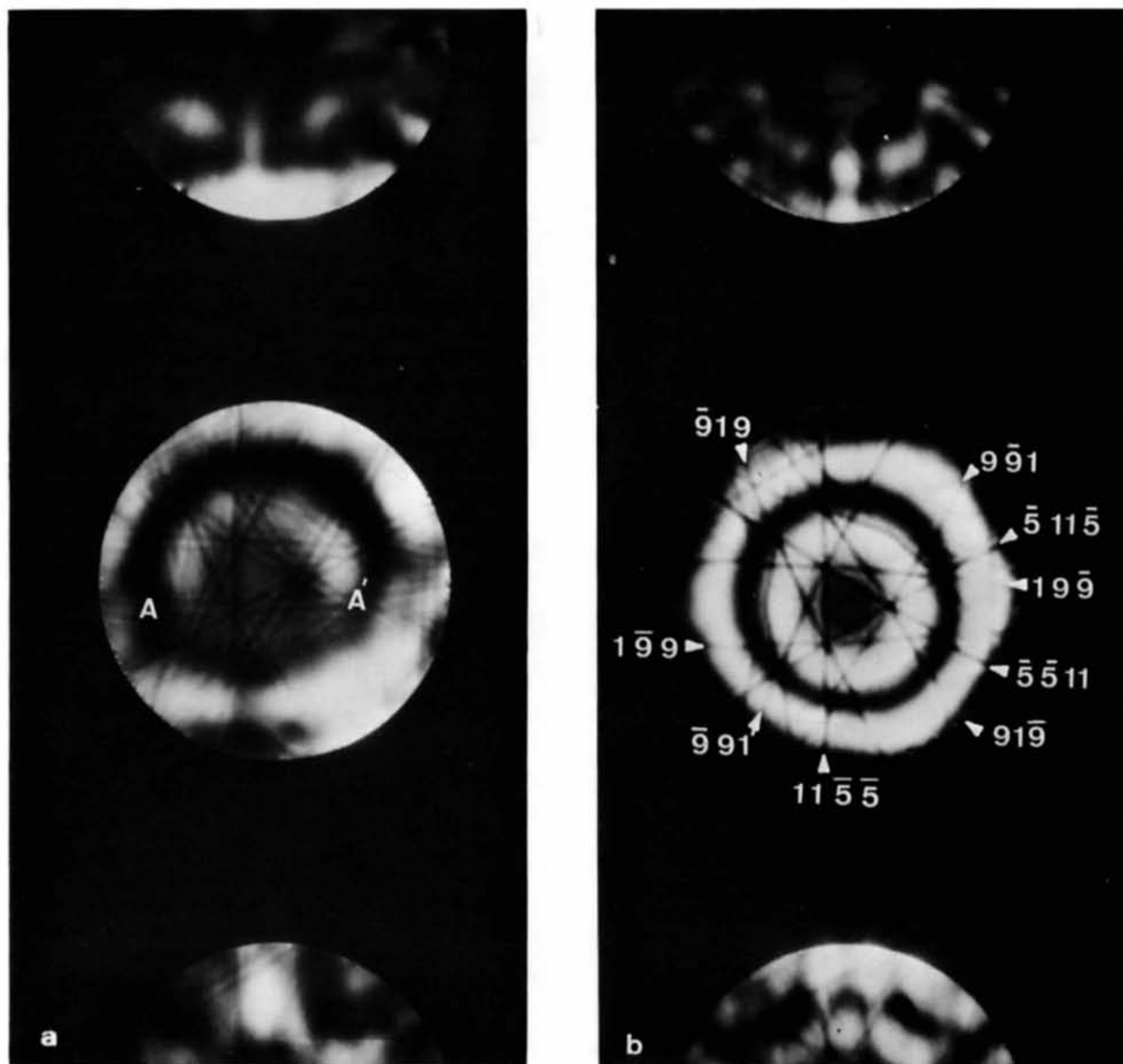

Fig. 2. CBED patterns with beam direction $\mathbf{B} = [111]$ in silicon taken at 100 kV from a dislocation (*a*) and from a perfect crystal (*b*). The indices of HOLZ lines of interest are noted on the perfect-crystal pattern. Pattern recorded with $L \simeq 1 \cdot 70$ m. The theoretical calculations in Fig. 9 show the intensity variation expected across a line such as AA'. $\mathbf{b} = \pm\frac{1}{2}[0\bar{1}1]$. The slight misorientation in (*a*) resulted from the presence of the dislocation.

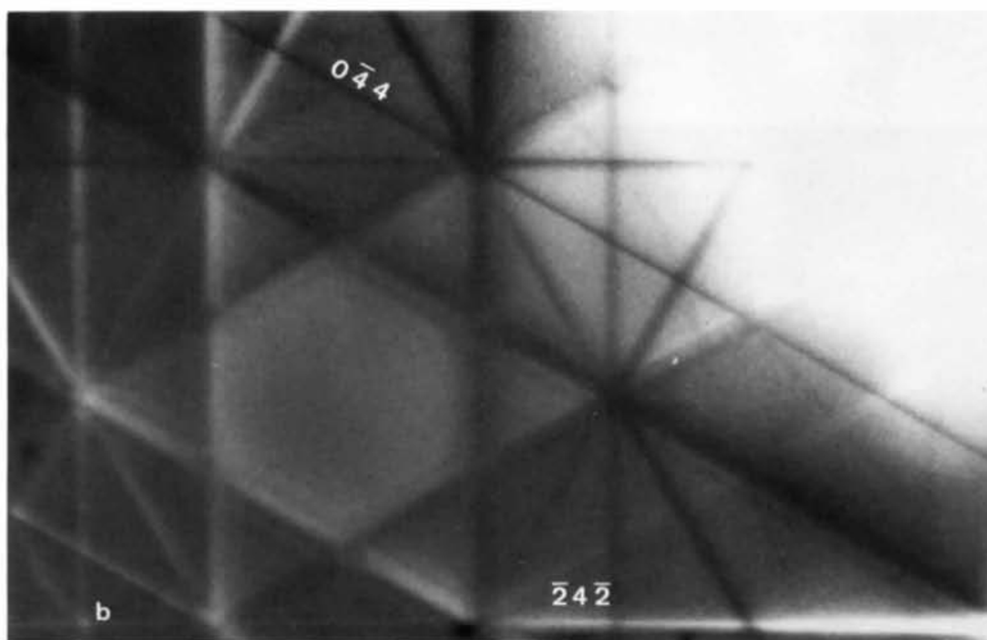

(*b*)

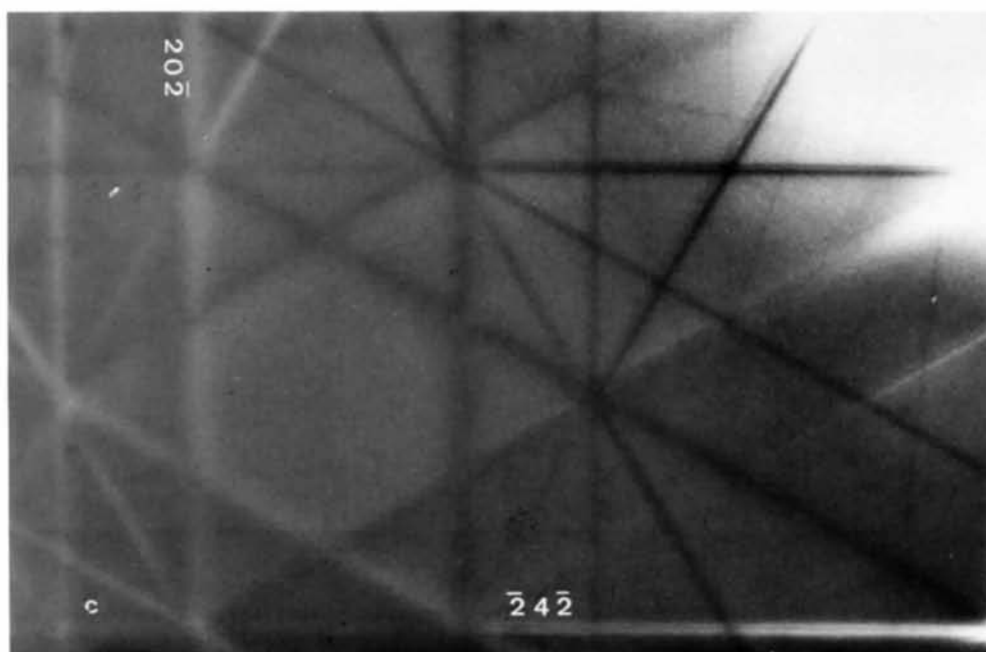

(*c*)

Fig. 7 (*cont.*) (*b*) CBED with probe on dislocation *D*. Note splitting on all $\langle hh0 \rangle$ Kikuchi lines and bands and unsplit $K[\bar{2}4\bar{2}]$. (*c*) CBED with probe on dislocation *E*. Note unsplit $[\bar{h}0h]$ and split $[24\bar{2}]$ Kikuchi lines; all other Kikuchi lines are split.

shows an example of two loops with different Burgers vectors whose CBED patterns were examined for a number of incident beam directions **B**. Diffraction contrast imaging experiments showed $\mathbf{b} = \pm\frac{1}{2}[10\bar{1}]$ for loop *A* and $\mathbf{b} = \pm\frac{1}{2}[\bar{1}10]$ for loop *B*. In Fig. 5(*a*) it can be seen that the Kikuchi bands corresponding to diffraction vectors normal to **b**, in or out of the [111] zone, are not observably split. However, all other Kikuchi bands, which are sensitive to the displacement field of loop *A*, are split. In this loop case, the splitting is much more complex than the straight single dislocations discussed above; here threefold and occasionally fourfold splitting was observed. Splitting is more pronounced in this case because the displacement field from the loop occupies a larger part of the irradiated crystal volume. When $\mathbf{B} = [211]$ (Fig. 5*b*) the $\pm[1\bar{3}1]$ Kikuchi bands are unsplit; in this case the Burgers vector of interest does not lie in the [211] zone, but rather makes an angle of 73° with the beam direction. Similarly, when $\mathbf{B} = [011]$ (Fig. 5*a*) the $\pm n[\bar{1}1\bar{1}]$ Kikuchi bands are not split, and **b** is 60° from the zone axis. The observations made on the absence of observable splitting for Kikuchi lines from Bragg spots in the zero and higher layers of the reciprocal lattice are consistent with the Burgers-vector analysis for loop *A*. Similar observations were made for loop *B*. Perfect-crystal [211] and [011] CBED patterns corresponding to those from loop *A* in Figs. 5(*b*),(*c*) are shown in Figs. 6(*a*),(*b*).

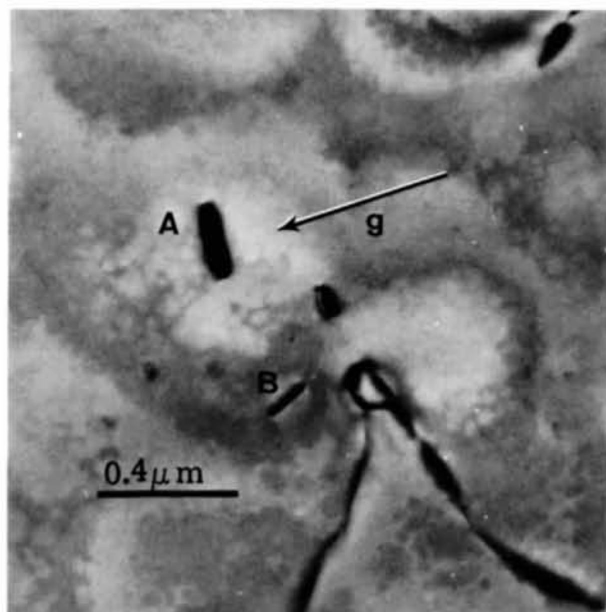

Fig. 4. Dislocation loops in silicon deformed at 1273 K. Loop *A* out of contrast for $\mathbf{g} = \pm[1\bar{1}1]$, $s > 0$ and $\mathbf{g} = \pm[1\bar{3}1]$. Residual contrast characteristic of this material is seen. Similar experiments show loop *B* has $\mathbf{b} = \pm\frac{1}{2}[110]$, $\mathbf{g} = [\bar{2}02]$.

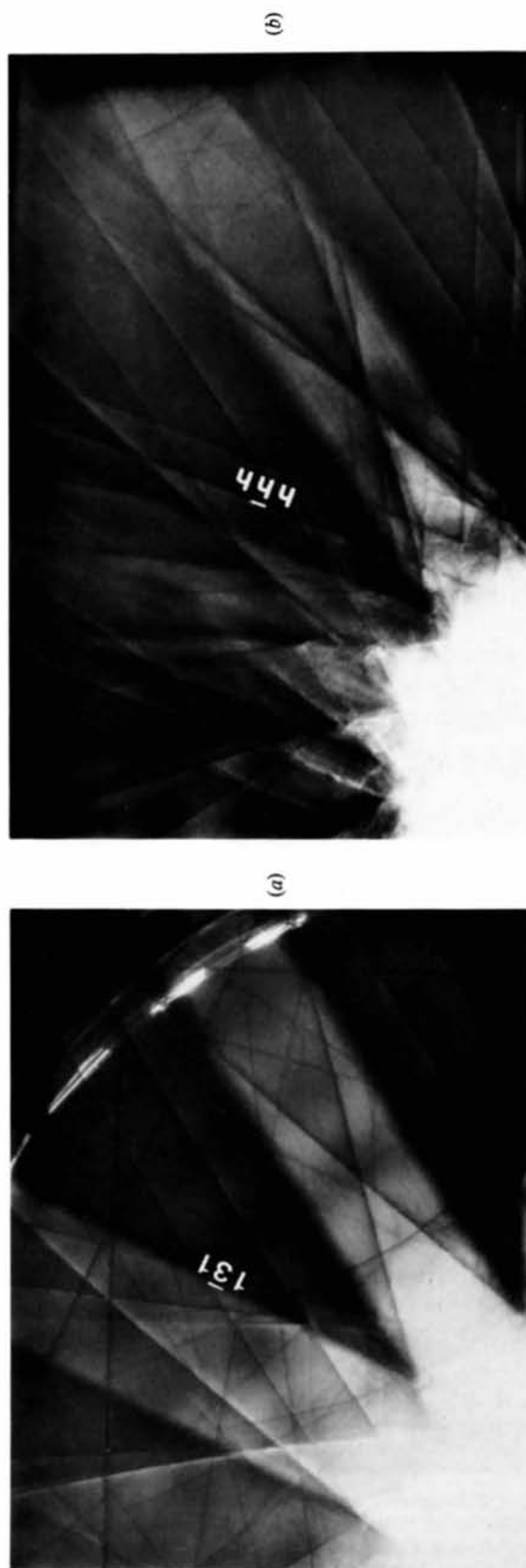

Fig. 6. (*a*),(*b*) Perfect-crystal [211] and [011] CBED patterns corresponding to those from loop *A* in Fig. 5 (*b*),(*c*).

In Fig. 7 we show CBED patterns from dislocations in aluminum. Several short inclined dislocations in aluminum were examined to evaluate the method in an elastically isotropic material with somewhat less sharply defined Kikuchi bands and lines than silicon. Typical results are shown in Fig. 7. The images and diffraction patterns were recorded with B about 2° from [111]; the foil thickness was 2450 Å ± 2% (Kelly, Jostons, Blake & Napier, 1975). The Burgers vector for the dislocation D, $\pm\frac{1}{2}[\bar{1}01]$, is in the [111] zone so that all the $\langle hk0 \rangle$ Kikuchi lines are split; the $\pm[\bar{2}4\bar{2}]$ Kikuchi lines correspond to diffraction vectors normal to the Burgers vector and are unsplit [Fig. 7(*b*)]. The Burgers vector for dislocation E, $\pm\frac{1}{2}[101]$, is out of the [111] zone; in this case the $\pm[\bar{h}0h]$ Kikuchi lines are unsplit and the $\pm[\bar{2}4\bar{2}]$ Kikuchi bands are split. All of these results are consistent with the conventional image Burgers-vector analysis of the dislocations. The CBED patterns shown here for aluminum were taken with the crystal slightly off the [111] zone axis to enhance the visibility of Kikuchi lines relative to the general diffuse background intensity. CBED patterns were obtained from aluminum equivalent to that shown in Fig. 1(*a*) for silicon, but the visibility of Kikuchi line fine structure was reduced, a result of the higher phonon background intensity when many strong Bragg reflections were excited.

4. Calculations

Techniques for the computation of convergent-beam patterns from imperfect crystals have received little attention in the literature. For dislocations, the only results appear to be those of Rez (1979), who has computed the effects of defects on the coarse 'rocking curve' structure in the central disk in the ZOLZ approximation [this structure is the set of broad rings in the central disk of Fig. 2(*b*)]. In this section we are interested in the modification to the fine HOLZ lines crossing the central disk due to defects [compare Figs. 2(*b*) and (*a*)]. These HOLZ lines are excluded in the ZOLZ approximation. Earlier calculations have also been reported for STEM microdiffraction patterns from dislocations based on the technique of periodic continuation (Spence, 1978); however, this method is unnecessarily accurate and time consuming for present purposes, in which contrast arises from the long-range strain field of the dislocation rather than from the detailed atomic arrangement at the core. Under these conditions the appropriate approximation is the column approximation, which neglects high-angle diffuse elastic scattering from heavily strained material (Anstis & Cockayne, 1979).

While forward calculations of CBED patterns from defects are no doubt possible with the column approximation, the approximations involved and the role of the

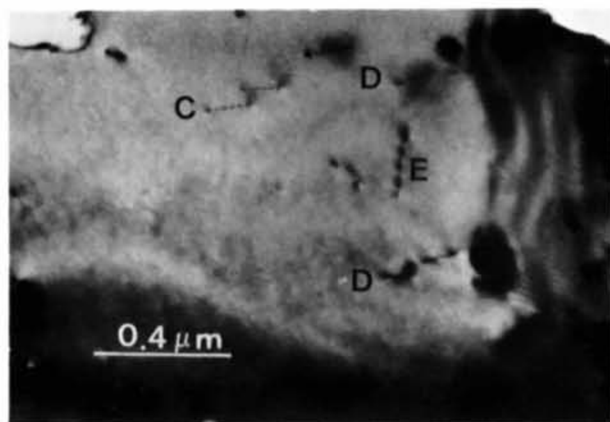

Fig. 7. Inclined dislocations near a grain boundary in polycrystalline aluminum deformed 3% at room temperature. (*a*) Bright-field image showing dislocations with three different **b** in contrast: for C, $\mathbf{b} = \pm\frac{1}{2}[0\bar{1}\bar{1}]$; for D, $\mathbf{b} = \pm\frac{1}{2}[\bar{1}01]$; for E, $\mathbf{b} = \pm\frac{1}{2}[101]$; $\mathbf{g} = [2\bar{2}0]$, $\mathbf{B} \simeq [111]$.

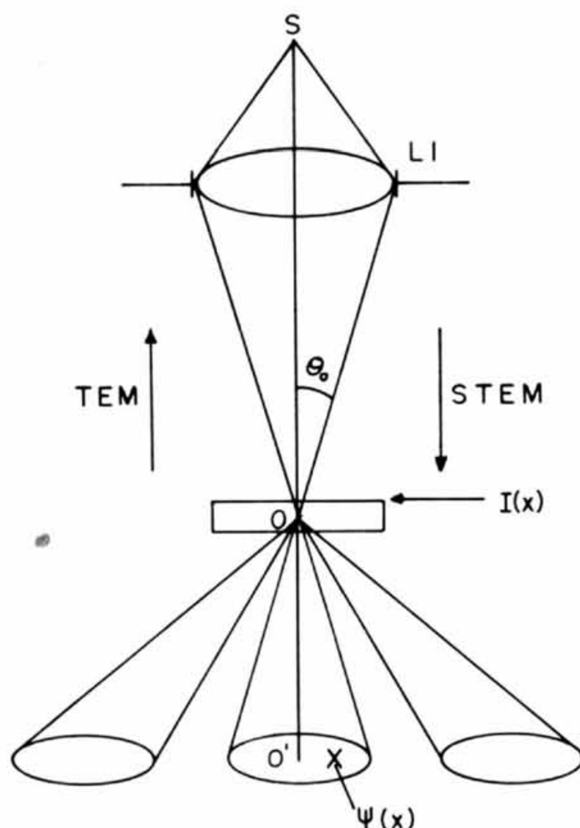

Fig. 8. Reciprocity diagram used for column approximation calculation of CBED from defects. The interchange of source (S) and detector (X) allows the CBED intensity at X to be obtained by calculating the TEM image contrast at S due to illumination from X.

electron probe size are more clearly revealed if the reciprocity argument (Cowley, 1975) shown in Fig. 8 is used. The interchange of source S and detector X in the figure allows the intensity in the convergent-beam disk at X to be computed under the column approximation by calculating the TEM image contrast which would be found at S owing to illumination from the off-axis point X below the specimen. This can be done with existing TEM diffraction contrast software based on the column approximation, since this supplies the value of the image intensity $I(x)$ at the specimen exit face (see Fig. 8).

The failure conditions of this approximation can be seen by considering the effect of using an extended source in STEM. Since this is equivalent to the use of an extended 'detector' (*e.g.* large-grained film) in TEM, the finite size of the electron probe in CBED can be incorporated by including an incoherent sum over the reciprocally related TEM image points which cover an area equivalent to the CBED field emission source size d. This local smoothing is achieved by forming

$$I'_x(x') = I(Mx) * h_d(x) = I(x) * h_p(x),$$

where $h_d(x)$ is a 'top-hat' function of width d, the $*$ denotes convolution, and p is the probe size at the specimen. The STEM magnification of lens $L1$ is $M = p/d$ (the TEM magnification is $1/M$). Here $I'_x(x')$ is both the locally averaged TEM image contrast at the image point x' due to illumination from X, and, through the reciprocity theorem, the CBED pattern intensity at X due to a probe centered at x' and formed by a source of size d. Now the estimate of $I(x')$ is limited in resolution through the use of the column approximation to, say, $c \simeq 1$ nm. Thus the local smoothing applied through the use of the column approximation will be unimportant if $p > c$. Conversely, we might expect this method of calculation to fail for CBED electron probe sizes smaller than the column width c. If the probe is diffraction limited and formed by an objective aperture of semiangle θ_0 (see Fig. 8), then $p \simeq \lambda/\theta_0$ and this condition limits the angular range of column approximation calculations in CBED to illumination semiangles $\theta < \theta_0 = \lambda/c$.

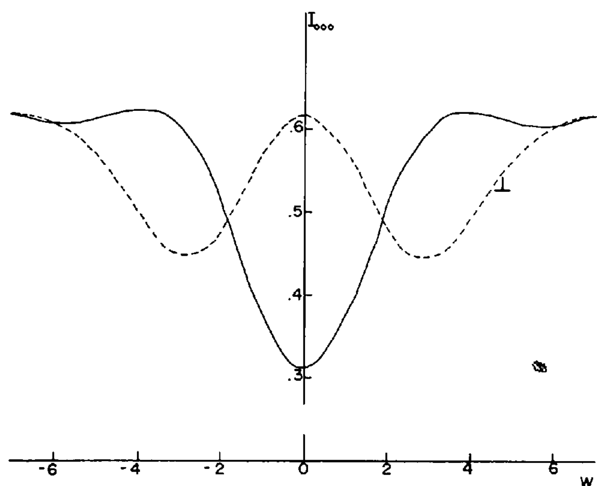

Fig. 9. Intensity variation across the [199] HOLZ line in the central CBED disk of a [111] zone-axis pattern from silicon at 120 kV calculated with two-beam theory and the reciprocity argument of Fig. 8 under the column approximation. The continuous line gives the intensity for a perfect crystal and shows a characteristic minimum as the Ewald sphere brushes through the $[1\bar{9}9]$ HOLZ reflection. The dashed line shows the effect of introducing a pure edge dislocation ($\mathbf{b} = \pm\frac{1}{2}[0\bar{1}1]$) under the probe. The slip plane is (111). The deviation parameter $W = S\xi_g$, where S is the $[1\bar{9}9]$ excitation error and $\xi_{1\bar{9}9}$ its extinction distance.

An accurate calculation of HOLZ-line splitting due to the presence of defects would require the inclusion of all HOLZ layers. This is possible in principle by extending either the expression of Tournarie (see, for example, Goodman & Moodie, 1974), or the perturbation technique of Buxton (1976) to incorporate the column approximation. Accurate values of the absorption coefficients, which are difficult to obtain, would also be needed in addition to accurate values of foil thickness and dislocation depth. Such a calculation has not been attempted for the present experimental conditions; however, the main features of the HOLZ line splitting are suggested by calculations based on the two-beam dynamical theory incorporating the column approximation. Through neglect of all ZOLZ interactions, this theory excludes the broad dark bands in the central disk of Fig. 2(*b*). The results of these calculations are shown in Fig. 9, where the computed intensity across the [199] HOLZ line in the central disk of the [111] CBED pattern is shown for both a perfect silicon crystal and one containing an edge dislocation on the slip plane normal to the electron beam. The Burgers vector $\mathbf{b} = \frac{1}{2}[0\bar{1}1]$ thus makes a small angle with the 'out-of-zone' reflection $\mathbf{g} = [1\bar{9}9]$. The HOLZ line is seen to be split into two subsidiary minima, in qualitative agreement with the experimental results of Fig. 2(*b*).

The orientation of the Ewald sphere for the reciprocally related TEM calculation shown here is defined by the direction XO (see Fig. 8). Unlike the case of reciprocity applied to centrosymmetric crystals in the zone-axis orientation (Pogany & Turner, 1968), in these three-dimensional defect calculations there are frequently no simplifying space-group symmetries which can be combined with the results of the reciprocity theorem. Methods of indexing the HOLZ line and Kikuchi patterns are discussed in Hirsch, Howie, Nicholson, Pashley & Whelan (1965), and the effects of strain on HOLZ patterns are further discussed in Jones, Rackham & Steeds (1977).

Table 1. *Effect of dislocations on CBED patterns from f.c.c. crystals*

Type of dislocation	Example (**b**)	Effect on CBED
In-zone unit dislocation	$\pm\frac{1}{2}[1\bar{1}0]$	$\pm[22\bar{4}]$ in-zone Kikuchi lines unsplit; all FOLZ Kikuchi and FOLZ lines in $[1\bar{1}0]$ zone unsplit
Out-of-zone unit location	$\pm\frac{1}{2}[110]$	$\pm[h\bar{h}0]$ in-zone Kikuchi lines unsplit; $[9\bar{9}1]$ FOLZ line unsplit
In-zone Shockley partial	$\pm\frac{1}{6}[\bar{1}\bar{1}2]$	$\pm[h\bar{h}0]$ in-zone Kikuchi lines unsplit; all FOLZ lines split
Out-of-zone Shockley partials	$\pm\frac{1}{6}[\bar{1}1\bar{2}]$	$\pm[6\bar{2}\bar{4}]$ in-zone Kikuchi lines unsplit
	$\pm\frac{1}{6}[121]$	$\pm[h0\bar{h}]$ in zone Kikuchi lines unsplit; $[11\bar{1}\bar{9}]$, $[\bar{9}\bar{1}11]$ FOLZ lines unsplit

5. Discussion

The HOLZ and Kikuchi lines in a CBED pattern, corresponding to many different Bragg reflecting planes in the zeroth- and higher-order Laue zones, have been shown to exhibit splitting according to whether or not the corresponding diffracting planes sense the displacement field of a dislocation. The Burgers vector was determined from a single CBED pattern from the Miller indices of unsplit lines. Since a single CBED pattern of high symmetry contains many HOLZ and Kikuchi lines, and each can be examined for the presence of splitting individually, the information content is higher than in two-beam image/diffraction pattern pairs. A CBED pattern with n beams excited, where n includes ZOLZ and HOLZ reflections, is more than equivalent to n two-beam images for determination of Burgers vectors because images are usually dominated by strong ZOLZ reflections only. Dislocation line directions must still be obtained from conventional diffraction contrast imaging experiments, since the elastic diffuse scattering in a diffraction pattern from a dislocation (which is normal to the dislocation line direction) is not usually visible in a CBED pattern.

These results suggest that convergent-beam patterns can be used in many cases to find fault vectors, including those with a component in the electron beam direction. This is a valuable technique if used in conjunction with high-resolution lattice imaging (where the goniometer tilt range is very limited), both for aligning specimens accurately before lattice imaging and for the determination of shear plane and dislocation fault vector components in the beam direction. For dislocations, our experimental results cover a few of the very many possible cases. These and other results to be expected are given in Table 1. In particular, we have not considered either highly anisotropic material or dissociated dislocations. For unresolved partials, where the partial separation is much smaller than the probe diameter (about 10 nm in our experiments) St Venant's principle can be used to show that no splitting is expected on lines for which $\mathbf{g}.\mathbf{b}_T = 0$, where $\mathbf{b}_T$ is the total Burgers vector. As the probe size is reduced and localized at a particular partial $\mathbf{b}_p$, lines for $\mathbf{g}.\mathbf{b}_T = 0$ will become increasingly disturbed, while those for which $\mathbf{g}.\mathbf{b}_p = 0$ appear unsplit.

CBED patterns from lattice defects in materials which are highly anisotropic are expected to contain more complex fringe patterns than those from silicon (12% anisotropy); the analogue of 'residual contrast' in imaging experiments (*i.e.* weak Kikuchi or HOLZ line fringes) is to be expected in some cases.

The authors are indebted to Mr Harry Kolar for preparation of the silicon specimens and Mr John Houston for preparation of the aluminum specimens. This work was supported by the Division of Material Sciences, US Department of Energy, under contract W-7405-eng-26 at Oak Ridge National Laboratory and by the National Science Foundation under grant No. DMR-77-2283.

References

ANSTIS, G. R. & COCKAYNE, D. J. H. (1979). *Acta Cryst.* A**35**, 511–524.

BUXTON, B. F. (1976). *Proc. R. Soc. London Ser. A*, **350**, 335–361.

CARPENTER, R. W. & BENTLEY, J. (1979). *Scanning Electron Microscopy*/1979/I, pp. 153–160. SEM, Inc., AMF O'Hare, IL60666, USA.

CHERNS, D. (1974). *Philos. Mag.* **30**, 549–556.

COWLEY, J. M. (1975). *Diffraction Physics.* Amsterdam: North-Holland.

GOODMAN, P. (1975). *Acta Cryst.* A**31**, 804–810.

GOODMAN, P. & MOODIE, A. F. (1974). *Acta Cryst.* A**30**, 280–290.

HIRSCH, P. B., HOWIE, A., NICHOLSON, R. B., PASHLEY, D. W. & WHELAN, M. J. (1965). *Electron Microscopy of Thin Crystals.* London: Butterworths.

JONES, P. M., RACKHAM, G. M. & STEEDS, J. W. (1977). *Proc. R. Soc. London Ser. A*, **354**, 197–222.

KELLY, P. M., JOSTONS, A., BLAKE, R. G. & NAPIER, J. G. (1975). *Phys. Status Solidi A*, **31**, 771–780.

POGANY, A. P. & TURNER, P. S. (1968). *Acta Cryst.* A**24**, 103–112.

RACKHAM, G. M. & STEEDS, J. W. (1976). Proc. EMAG 75, Univ. of Bristol, 8–11 September 1975, pp. 457–460.

REZ, P. (1979). *Proc. 36th Annual Electron Microscopy Society of America Meeting*, pp. 438–439. Baton Rouge: Claitor.

SPENCE, J. C. H. (1978). *Acta Cryst.* A**34**, 112–116.

STEEDS, J. W. (1979). *Introduction to Analytical Electron Microscopy*, edited by J. J. HVEN, J. GOLDSTEIN & D. JOY, p. 387. New York: Plenum.